Energy Conversion and Management 308 (2024) 118395

Contents lists available at ScienceDirect

Energy Conversion and Management

journal homepage: www.elsevier.com/locate/enconman

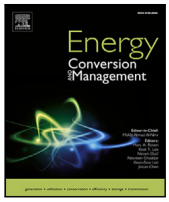

Research Paper

Development and validation of a phenomenological model for hydrogen fueled PFI internal combustion engines considering Thermo-Diffusive effects on flame speed propagation

V. De Bellis [a], M. Piras [a], F. Bozza [a], E. Malfi [a,*], R. Novella [b], J. Gomez-Soriano [b], M. Olcina-Girona [b]

[a] Industrial Engineering Department, Mechanic and Energetic Section, University of Naples "Federico II", via Claudio 21, 80125 Naples, Italy
[b] CMT - Clean Mobility & Thermofluids, Universitat Politècnica de València, Camino de vera s/n, 46022 Valencia, Spain

ARTICLE INFO

Keywords:
Hydrogen
Hydrogen combustion
0D/1D ICE model
Model validation

ABSTRACT

This paper proposes a 1D numerical/experimental study on a single-cylinder research ICE equipped with a hydrogen Port Fuel Injection (PFI) system. The experimental campaign covered tests at the fixed speed of 1500 rpm and different levels of load, from 5 bar to 11 bar IMEP, and of air excess, with a relative air-to-fuel ratio ranging from 1.4 to 4.0. A 0D/1D model of the investigated ICE is developed, including detailed combustion, turbulence, and NO_x emission sub-models. In particular, combustion model is based on the fractal approach, k-K-T model is adopted for describing turbulent phenomena and NO_x emissions are predicted by the Zeldovich mechanism. A sub-model was developed to assess the influence of Thermo-Diffusive (TD) instabilities on the freely propagating flame speed accounting for equivalence ratio, variable transport coefficients and reaction orders. This evaluation considered the impact of TD instabilities commonly observed in lean premixed hydrogen combustion on the flame front. The engine model calibration process enabled the comparison between numerical predictions and experimental observations, encompassing pressure cycles, burn rate traces, and main engine performance (air flow rate, IMEP, indicated efficiency, and timing of main combustion events). The model replicated the IMEP with an average error of 2.5%, gross indicated efficiency with an average error of 1.6%, main combustion angles with an average error of 3.8 CAD on CA_{50}, and NO_x emissions satisfactorily, showing high sensitivity to operational parameters. Nonetheless, less accurate predictions occur in cases with significantly elevated λ values ($\lambda > 3.6$), which were attributed to the presence of thickened flames, where some assumptions inherent to the adopted combustion model may fail. Finally, a comparison between the proposed approach and the one proposed in Ballerini et al. (2022) is presented, and readers are provided with recommendations for further development of future models that account for Thermo-Diffusive instabilities in lean hydrogen combustion.

1. Introduction

The transportation sector significantly contributes to greenhouse gas and air pollutant emissions, primarily due to internal combustion engines (ICEs) emitting harmful substances like NO_x, PM, and CO [1]. To address this issue, regulations, especially in Europe, aim to reduce CO_2 emissions by specific targets. Solutions involve lower-carbon fuels and alternative vehicles like battery electric vehicles (BEVs) and hydrogen-powered vehicles [2–4]. Hydrogen shows promise for decarbonization in sectors such as heavy-duty transportation and power generation, complementing BEVs, particularly in high-load and long-distance applications [5–7]. Hydrogen ICEs can achieve high power density levels while concurrently maintaining remarkably low tailpipe emissions. Nevertheless, despite these advantages, these engines may still generate trace amounts of hydrocarbons due to excess oil consumption. The primary concern in terms of emissions remains the presence of NO_x, as substantiated by various research studies [8–11]. The heightened production of NO_x is a consequence of the rapid combustion rate and the resulting elevated temperatures, characteristics intrinsic to the chemical properties of hydrogen. To mitigate these emissions, two main approaches are followed. Firstly, the wide flammability range and low ignition energy of hydrogen enable the engine to operate at exceedingly lean equivalence ratios, thereby effectively reducing the flame temperature and, consequently, NO_x emissions. Secondly, the

* Corresponding author.
E-mail address: enrica@unina.it (E. Malfi).

https://doi.org/10.1016/j.enconman.2024.118395
Received 10 January 2024; Received in revised form 11 March 2024; Accepted 3 April 2024
Available online 9 April 2024

introduction of Exhaust Gas Recirculation (EGR), often in the form of water vapor, serves as an additional mechanism to curtail engine-out NO_x levels, a strategy outlined in various research works [12–14]. For any residual emissions that may persist, the implementation of suitable after-treatment devices represents an effective solution to effectively solve the problem [15].

Furthermore, when operating with lean combustion, lean premixed hydrogen flames exhibit thermo-diffusive instabilities, a phenomenon rooted in the fuel's high mobility, leading to localized acceleration and flame thinning. Excluding the influences of turbulence, acoustics, and buoyancy effects, lean premixed hydrogen flames reveal two significant instabilities: the Darrieus–Landau instability and the thermo-diffusive instability. The former arises due to the density decrease attributed to heat release across the flame, while the latter originates from an imbalance between thermal and molecular diffusion. Robust experimental evidence supports the existence of these instabilities [16,17]. To comprehend the thermo-diffusive instability's occurrence, the Lewis number of the reactants can be examined, which quantifies the ratio between thermal diffusivity and the molecular diffusivity of the chemical species. When molecular diffusion exceeds thermal diffusivity ($Le < 1$), the flame front experiences acceleration in regions where it is convex toward the fresh gases. This leads to an increase in local flame speed, resulting in a thinner flame front and higher temperature compared to the reference laminar, planar, steady, and unstretched flame. Conversely, when the flame front is convex toward the burnt gases, the flame velocity decreases relative to the reference laminar flame speed, causing the flame to thicken, and the temperature to decrease. This creates an unstable condition where the flame front becomes wrinkled, resulting in an increase in flame speed and the formation of chaotic burning cells. These cells are separated by regions of near extinction, resulting in the so-called "cellular burning" or the self-turbulent propagation regime. More recent studies demonstrated that a strong interaction between hydrogen instabilities and turbulence exists [18]. In this study, a significantly higher stretch factor, $I_0 = 4$, was observed in the turbulent flame, whereas a value of $I_0 = 2.6$ was obtained in the laminar thermo-diffusive unstable flame. These results indicate that TD instabilities persist in turbulent flows and even exhibit synergistic interactions with turbulence, which must be considered in turbulent combustion models.

For the preliminary assessment of hydrogen-powered engines' performance, the utilization of computational tools plays a pivotal role. These tools allow in-depth insights into critical aspects, including mixture preparation and the combustion process. Furthermore, they facilitate a comprehensive system optimization process [19]. In a study conducted by Klepatz et al. [20], a comprehensive methodology was presented, wherein a one-dimensional Computational Fluid Dynamics (CFD) model of the H_2-ICE was validated using experimental data. This validated model was subsequently employed to conduct a comparative analysis of the efficiency of various engine concepts. The combustion model employed is based on a modified Wiebe approach, thus exhibiting limited predictive capabilities. Building upon this foundational research, a subsequent study [21] extended this methodology to optimize the calibration of a hydrogen-revamped diesel engine. Moreover, it investigated the potential benefits of EGR on both the performance and emissions of the engine, providing valuable insights into advanced engine development and emissions reduction strategies. In the literature, there are also 0D/1D and 3D predictive models available for the H_2-ICE. The article by Millo et al. [22] explored the conversion of a 3.0 L diesel engine into a hydrogen-fueled SI engine, highlighting the potential benefits of hydrogen as an alternative fuel. The study used a combination of zero-, one-, and three-dimensional CFD approaches to evaluate hydrogen combustion and NO_x emissions. Without significant modifications to the turbocharger and combustion systems, the converted engine achieved a power density of 34 kW/L and a maximum brake thermal efficiency (BTE) of approximately 42%. Based on the same modeling approach, in [23] the authors explored the potential of a comprehensive quasi-dimensional model designed for H_2-ICE. The combustion model, named SITurb, incorporated modifications for laminar flame speed determination, a chemistry-based knock model, and a cycle-by-cycle variability (CCV) model. Validation against experimental data from a 0.5 L PFI single-cylinder engine demonstrated the model's ability to accurately simulate the combustion process, including CCV, and predicted the occurrence of knocking cycles during various spark sweeps. The studies listed above have considered a maximum λ of 2.5 and have not taken into account thermo-diffusive instabilities, the effects of which become increasingly evident as λ increases. In [24], authors numerically explored full load operating conditions of an H_2-ICE operating at λ up to 3. This study aimed to enhance a 1D thermo-fluid dynamic simulation code for H_2-ICE. It refined the combustion modeling by replacing the correlation-based approach for laminar flame speed, validated for $0.2 \leq \lambda \leq 3$, with a Tabulated Kinetic method and incorporated correction factors to account for surface instabilities derived from [25]. These enhancements were validated by comparing in-cylinder pressure trends and intake/exhaust pressure pulses with experimental data. The model introduced by Howarth et al. [26,27] constitutes an attempt to simultaneously address both laminar and turbulent flame speeds using a constrained one-dimensional speed. This correction is achieved by incorporating the effects of thermo-diffusive instability in the laminar flame speed through straightforward algebraic closures. Differently from [24], the interactions between TD instabilities and turbulence are modeled too. However, it is worth noting that this approach has not been validated within the context of 0D/1D simulations of hydrogen-fueled ICEs. In this article, a 1D numerical/experimental study of a single-cylinder research ICE operating at relative air-to-fuel ratios ranging from 1.4 to 4.0 and equipped with a hydrogen PFI system is proposed. Initially, a novel correlation for determining the laminar flame speed of hydrogen is formulated through planar flame thermo-chemical calculations. Subsequently, a model is developed to assess the influence of thermo-diffusive instabilities on the freely propagating flame speed. A turbulence model is tuned through the utilization of data obtained from a 3D simulation, facilitating the optimization of the combustion model. This calibration process enabled a comparison between numerical predictions and experimental observations, including pressure cycles, burn rate profiles, and overall engine performance parameters. Finally, a comparison between the proposed approach and the one adopted in [24] is presented, highlighting possible developments to enforce model predictive capabilities, especially for the extreme lean air/hydrogen mixtures. Hence, the primary novelty of this paper lies in the development and validation of a phenomenological model capable of predicting engine performance with ultra-lean conditions, in air/hydrogen proportions never explored in the current literature, while considering the thermodynamic instabilities occurring in this combustion regime and its interaction with turbulence.

Table 1
Engine characteristics.

Engine characteristics	
Engine type	4 stroke, 4 valves, PFI
Number of cylinders	1
Displaced volume [cm^3]	454.2
Stroke [mm]	86
Bore [mm]	82
Compression ratio	10.7:1

2. Engine details and experimental tests

The CMT — Clean Mobility & Thermofluids Research Institute in Valencia, Spain, tested a single-cylinder spark ignition research engine with a gaseous PFI system. The main features of the engine are listed in Table 1.

The schematic in Fig. 1 demonstrates the setup of the experimental test cell. It highlights specific locations for measuring pressure and

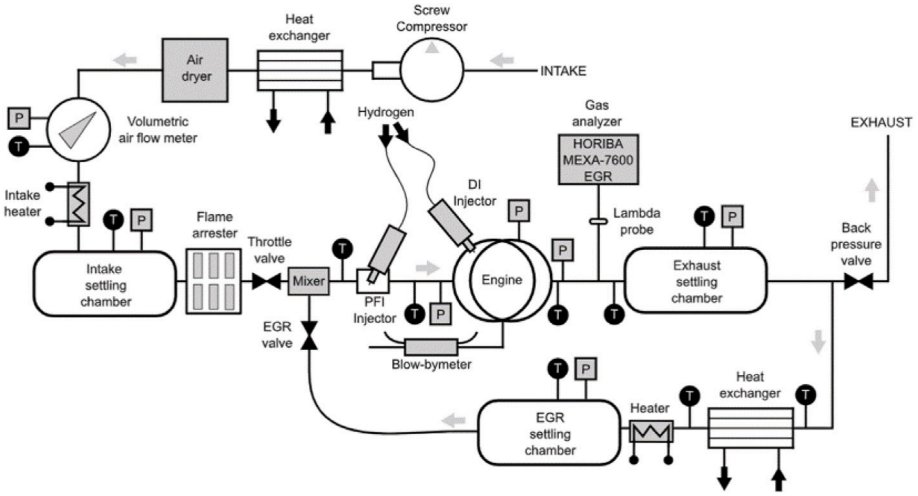

Fig. 1. Test cell diagram.

Table 2
Variable measured and devices used.

Signal (High frequency)	Sensor	Specification
In-cylinder pressure	Piezoelectric sensor	0 to 250 bar ± 0.3% linearity
Intake pressure	Piezoresistive sensor	0 to 10 ± 0.001 bar
Exhaust pressure	Piezoresistive sensor	0 to 10 ± 0.001 bar
Variable (Low frequency)	**Sensor**	**Specification**
Engine speed	Optical angular encoder	1 to 6000 ± 1 rpm
Engine torque	Strain-gauges torque-meter	−200 to 200 ± 1 N m
Intake pressure	Piezoresistive transducer	0 to 10 bar ± 1%
Exhaust pressure	Piezoresistive transducer	0 to 10 bar ± 0.3%
Intake temperature	Thermocouple type K	0 to 1000 ± 0.5 °C
Exhaust temperature	Thermocouple type K	0 to 1000 ± 0.5 °C
Fluid temperature	Pt100 thermoresistance	−200 to 850 ± 0.3 °C
Air mass flow	Air flow meter	0.6-100 m^3/h ± 1%
Hydrogen mass flow	Thermal mass flow meter	200–1600 l/min (based on N_2) ± 0.5%

temperature, fuel injection, as well as other control and measurement instruments. In-cylinder pressure data was collected using a Kistler piezoelectric transducer, while piezoresistive pressure sensors were employed to measure average flow pressures. Air mass flow was quantified using a volumetric airflow meter manufactured by Kromschroeder, while a Bronkhorst F-113AC-1M0-AAD-55-V flow meter was employed to register hydrogen mass flow. NO_x emissions produced during the combustion process were continuously monitored using a HORIBA MEXA-7600EGR gas analyzer (min. 0 to 10 ppm, max. 0 to 10 kppm, accuracy ±3%). To control intake pressure and temperature, auxiliary systems such as an external compressor and air conditioning system were used in conjunction with the engine's operational settings. Additionally, a knife-gate valve was implemented to replicate the desired exhaust backpressure. An overview of the instrumentation utilized and the precision of certain pertinent devices can be found in Table 2.

In the experiments, the hydrogen utilized was stored in pressurized tanks and directed into an injector after passing through a pressure discharge control system. Specifically, the injector employed in this scenario is the Zavoli JET Injector, specially designed for gaseous fuels. It operates within a maximum working pressure of 4.5 bar, maintains a working temperature range of −40 °C to 120 °C, and features a discharge nozzle with a diameter of 3 mm. Some relevant information concerning the properties of the fuel can be found in Table 3.

To ensure the stability of key parameters such as IMEP, Heat Release Rate (HRR), and combustion phasing, the test facility utilizes online combustion diagnostic software called INDICOM. Cycle-to-cycle variability is assessed by calculating the coefficient of variance of IMEP (CoV_{IMEP}), with steady-state engine operation achieved when CoV_{IMEP} remains below 5%. Each operating condition is subjected to

Table 3
Hydrogen properties.

Chemical formula	H_2
Autoignition temperature [K]	858
Mass diffusivity in air [cm^2/s]	0.61
Cetane number [–]	55.7
RON [–]	130
MON [–]	62-64
Lower heating value [MJ/kg]	119.9
Purity [%]	99.9

measurement at least three times, with 250 cycles recorded during each run to ensure an adequate dataset for subsequent thermodynamic analysis. For a more comprehensive understanding of the test facility equipment and methodology, reference can be made to prior research works [28].

The experimental measurements conducted for this study cover a spectrum of operating conditions, including IMEP values spanning from 5 to 11 bar, λ values ranging from 1.4 to 4.0, and spark timings varying from −36 to 0 CAD aTDC, as detailed in Table 4. The inclusion of this different range of conditions will ensure that the combustion model effectively captures the trends and detects the effects of the analyzed external parameters in this investigation. The investigation refers to a single engine rotational speed of 1500 rpm. This is the regime in which an engine of these characteristics (in its equivalent multi-cylinder version) typically operates under real driving conditions [29]. An error analysis has been conducted to estimate the error of the IMEP, according to [30]. The estimations were performed under the assumption of neglecting any measurement errors of the cylinder volume and

Table 4
Case study parameters.

Case	IMEP (bar)	λ (–)	ST (aTDC)	T_{intake} (K)	p_{intake} (bar)
1	4.74	1.4	−2.0	307.9	0.84
2	4.87	1.6	−4.2	305.9	0.90
3	4.97	1.8	−8.0	310.1	0.97
4	5.06	2.0	−12.2	316.3	1.05
5	5.13	2.2	−16.2	316.0	1.12
6	5.13	2.4	−20.0	314.9	1.19
7	5.20	2.6	−20.0	315.4	1.26
8	5.22	2.8	−24.2	316.2	1.35
9	5.24	3.0	−28.2	314.4	1.42
10	5.25	3.2	−30.2	314.1	1.49
11	5.22	3.4	−32.0	312.6	1.56
12	5.17	3.6	−30.0	312.0	1.62
13	5.08	3.8	−36.2	311.2	1.70
14	4.80	4.0	−36.2	311.4	1.75
15	8.47	2.4	−24.2	313.7	1.87
16	8.46	2.6	−26.0	314.4	1.98
17	8.65	2.8	−28.2	313.7	2.08
18	8.71	3.0	−32.0	312.5	2.23
19	8.69	3.2	−34.2	312.4	2.36
20	8.60	3.4	−36.2	312.2	2.43
21	11.22	2.6	−30.2	313.1	2.57

considering the TDC offset as zero, revealing an average error band of ±0.015 bar for the low load points (test cases 1 to 14), ±0.026 bar for the medium load points (test cases 15 to 20), and ±0.034 bar for test case 21.

3. Numerical approaches

In this study, the engine model employed is built in the commercial 1D simulation software GT-Power. Standard components from the software library are utilized to compute the intake and exhaust flows. To capture the in-cylinder processes, custom sub-models developed in-house are integrated into the 1D code. The combustion phenomena are modeled according to the fractal approach, briefly recalled in Section 3.4, while the in-cylinder flows and turbulence characteristics are modeled by the K-k-T model, deeply investigated in previous works [31,32]. This model is based on the solution of the balance equations of mean flow kinetic energy, K, turbulence kinetic energy, k, and tumble momentum, T. The K-k-T model describes the energy cascade mechanism from K to k, the energy production and destruction due to intake and exhaust valve flows, the tumble motion generation during intake and speed-up towards the TDC, which reflects in the turbulence local increase, and the degradation of k due to viscous effects. The dissipation rate of turbulence is not described by a dedicated balance equation, but derived from integral length scale evolution, L_i. This last is modeled as a sequence of S-shape functions, whose control points are assigned to fit the corresponding 3D trend. These in-house sub-models are meticulously designed to accurately represent the relevant phenomena. The operational parameters from the experimental engine are inputted into the 1D simulation framework. More specifically, valve actuation and discharge coefficients, pressure at intake and exhaust environments, fuel flow rate, and the spark advance are specified in the model. Additionally, user routines containing correlations for laminar flame speed (Section 3.2) and the effects of flame instabilities (Section 3.3) are integrated into the software to enhance its predictive capabilities. The in-cylinder wall heat transfer is simulated based on the Woschni-like correlation.

3.1. 3D CFD model

To calibrate the phenomenological K-k-T flow and turbulence model, calculations of in-cylinder fluid dynamics were performed under motoring conditions using a 3D-CFD model created with the CONVERGE software. The construction of the 3D model employed a hexahedral grid approach based on an orthogonal foundation, as visualized in Fig. 2. The meshing of the computational domain utilized a base cell size of 4 mm, with refinement to 2 mm in the intake and exhaust regions and further refinement to 1 mm within the cylinder region. In order to capture fine details in proximity to the cylinder walls, including the moving piston and valves, cell resolution was increased to 0.5 mm. Furthermore, an Adaptive Mesh Refinement (AMR) algorithm was employed to enhance grid resolution in regions characterized by significant velocity and temperature gradients. The AMR algorithm incorporated sub-grid criteria of 1 m/s and 2.5 K, reducing cell size to a minimum of 0.125 mm. Comprehensive information concerning grid definition can be located in Table 5.

Table 5
Details of the mesh configuration.

Configuration	Size (mm)
Base size	4
Intake/exhaust ports	2
Chamber refinement	1
Walls refinement	0.5
AMR min. size	0.125
Number of cells	0.5–4 million

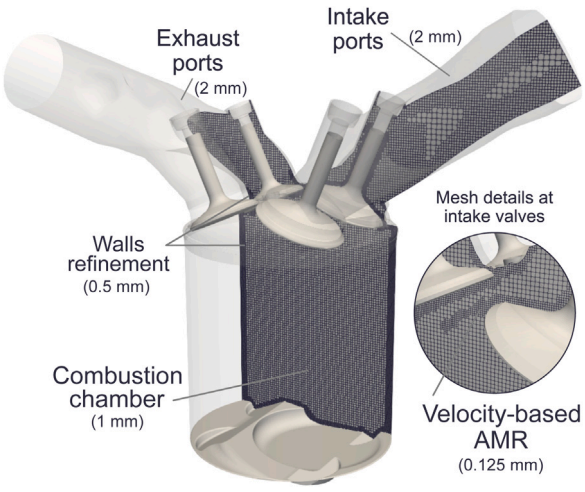

Fig. 2. General view of the mesh domain.

The turbulence modeling was conducted within the framework of unsteady Reynolds-averaged Navier–Stokes (URANS). Specifically, the Re-Normalization Group variant of the k-epsilon model (RNG k-ϵ model [33]), which is based on a two-equation turbulence model relying on eddy viscosity, was employed. The modeling of gas-to-wall heat transfer followed the approach proposed by Berni et al. [34], a method widely utilized in internal ICE applications. Spatial discretization in the simulations was accomplished using a second-order central difference scheme, while temporal discretization employed a first-order scheme. The coupling of pressure and velocity fields was realized by applying a modified Pressure Implicit with the Splitting of Operators (PISO) algorithm, as developed by [35]. Compressible flow properties were determined utilizing the ideal gas equation of state.

Validation of the 3D CFD model was performed against experimental data, with a comparison between the experimental results and CFD outcomes at 3000 RPM and 11 bar provided in [36]. Also, a similar mesh configuration has been widely used by other authors demonstrating the accuracy of the model to predict in-cylinder pressure and heat release rate in multiple engines and operating conditions [36–38].

3.2. Hydrogen laminar flame speed modeling

Throughout this research, a novel correlation for the laminar flame speed of hydrogen has been developed. This correlation was derived by

Table 6
Coefficients and reference conditions for S_L correlation.

Coefficients	
a	16.693
a1	35.265
a2	−85.431
a3	−72.679
a4	11.973
b	3.289
b1	0.722
b2	2.776
b3	3.767
b4	2.198
c	3.901
Reference conditions	
T, K	300
p, bar	1

fitting the results obtained from a chemical kinetics solver, CANTERA, applied to 1D planar laminar flames. The CANTERA calculations were carried out using the Konnov mechanism [39], which consists of 5 elements, 15 species, and 75 reactions. These calculations encompass a range of values for pressure (p), temperature (T), equivalence ratio (ϕ), and residual gas mass fraction (x_r), relevant to typical engine operations. The parameter ranges considered are as follows:

- Pressure: 1–120 bar
- Temperature: 600–850 K
- Equivalence ratio: 0.25–1
- Exhaust gas mass fraction: 0–0.25

For each set of conditions, the composition of the residual gas is determined based on the equilibrium composition of the combustion products. The resulting laminar flame speed (S_L) correlation is expressed as:

$$S_L = a\left(a_1\phi^3 + a_2\phi^2 - a_3\phi^3 - a_4\right) \times \left(\frac{T}{T_{ref}}\right)^b \left(\frac{p}{p_{ref}}\right)^{\left(b_1\phi^3 - b_2\phi^2 + b_3\phi^3 - b_4\right)} \times e^{cx_r} \quad (1)$$

The values of the correlation constants that provide the best fitting of the S_L data are listed in Table 6.

The coefficient of regression is 0.99 and the comparison between results from Eq. (1) are depicted in Fig. 3 for different levels of temperature and equivalence ratio.

3.3. Thermo-diffusive instability measurement

As described in the introduction, lean hydrogen flames are subjected to intrinsic instabilities. The combustion model has been appropriately adjusted to consider their impact on combustion evolution. The strengths of both Darrieus–Landau (DL) and thermo-diffusive instabilities are influenced by a variety of factors, including the properties of reactants, products, and the underlying chemistry. Consequently, it becomes essential to assess how flame instability responds to the local mixture state, allowing for proper model adjustments.

Initially, efforts to characterize DL instability involved the utilization of linear stability analysis, under the assumption of an infinitely thin flame. This analysis applied Rankine–Hugoniot jump conditions to the linearized Euler equations.

A comprehensive derivation of the dispersion relation can be found in Ref. [40]. It was observed that assuming the flame to be of the form $F(x,t) = Ae^{(\omega t + ikx)}$, propagating at a speed S_L with a characteristic thickness δ_L (and timescale $\tau_L = \delta_L/S_L$), the normalized growth rate of the instability, denoted as $\tilde{\omega}$, follows a dispersion relation:

$$\tilde{\omega} = \frac{1}{\sigma+1}\left(\sqrt{\sigma^3+\sigma^2-\sigma}-\sigma\right)\tilde{k} \quad (2)$$

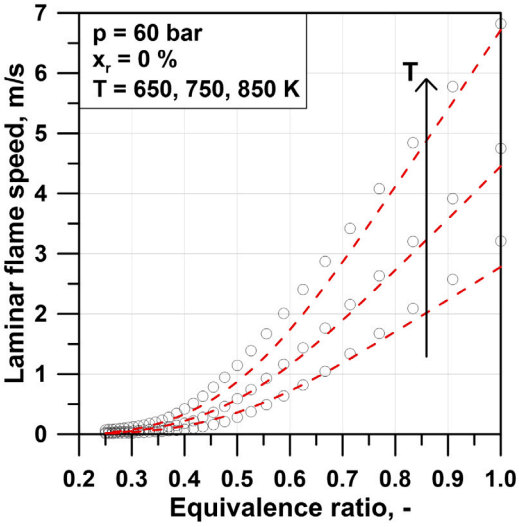

Fig. 3. Hydrogen laminar flame speed comparison between Eq. (1) (red line) and 1D plane flame speed from Cantera (circle).

Here, $\tilde{k} = k\delta_L$ represents the normalized wavenumber, and $\sigma = \frac{\rho_u}{\rho_b}$ denotes the density ratio across the flame. Nonetheless, this growth rate anticipates an unrestricted escalation concerning the wavenumber, a prediction that contradicts both experimental and computational findings. Furthermore, it fails to consider the influences of viscosity and diffusion, both of which have been established as significant factors in the initiation of thermo-diffusive instability. To address these limitations, a novel dispersion relation was formulated, encompassing the destabilizing effects of diffusion through the flame [41]. This revised relation introduces a second-order term, denoted as $\tilde{k}^2$, wherein ω_{DL} is determined by the equation $\omega_{DL} = \frac{1}{\sigma+1}\left(\sqrt{\sigma^3+\sigma^2-\sigma}-\sigma\right)$.

$$\tilde{\omega} = \omega_{DL}\tilde{k} + \omega_2\tilde{k}^2 \quad (3)$$

The studies outlined in [26,27] highlighted the significance of the coefficient ω_2 in effectively describing the thermally diffusive behavior exhibited by lean hydrogen flames. To offer a more inclusive analysis, encompassing factors such as equivalence ratio, variable transport coefficients, and reaction order, Matalon et al. [41] introduced a comprehensive expression for ω_2:

$$\omega_2 = -\left(B_1 + \beta\left(Le_{eff} - 1\right)B_2 + PrB_3\right) \quad (4)$$

where B_i are constants depending on the density ratio (σ) and temperature-dependent thermal conductivity (λ), β is the Zeldovich number of the reaction and Pr is the Prandtl number. Assuming unity reaction orders, the effective Lewis number of the unburned mixture is given by:

$$Le_{eff} = \begin{cases} \frac{Le_0 + ALe_f}{1+A}, A = 1 + \beta\left(\phi^{-1} - 1\right) if \phi < 1 \\ \frac{Le_f + ALe_0}{1+A}, A = 1 + \beta\left(\phi - 1\right) if \phi > 1 \end{cases} \quad (5)$$

The coefficients B_i, as originally defined by Matalon [42], are dependent on the thermal conductivity distribution within the flame. These functional expressions are explicitly a function of σ and are constructed through an integral that is contingent on the scaling of thermal conductivity ($\tilde{\lambda} = \lambda/\lambda_u$) concerning the normalized temperature ($x = T/T_u$). The complete mathematical expressions are presented as follows:

$$B_1 = \frac{\sigma}{2\left(\sigma + (\sigma+1)\omega_{DL}\right)} \times \left(\frac{\sigma(2\omega_{DL}+\sigma+1)}{\sigma-1}\int_1^\sigma \frac{\tilde{\lambda}(x)}{x}\,dx \int_1^\sigma \tilde{\lambda}(x)\,dx\right) \quad (6)$$

$$B_2 = \frac{\sigma(1+\omega_{DL})(\sigma+\omega_{DL})}{2(\sigma-1)\left(\sigma+(\sigma+1)\omega_{DL}\right)} \int_1^{\sigma} \log\frac{\sigma-1}{x-1}\frac{\tilde{\lambda}(x)}{x}\,dx \tag{7}$$

$$B_3 = \frac{\sigma}{\sigma+(\sigma+1)\omega_{DL}}\left((\sigma-1)\tilde{\lambda}(\sigma) - \int_1^{\sigma}\tilde{\lambda}(x)\,dx\right) \tag{8}$$

Crucially, the computation of the scaling function $\tilde{\lambda}$ for each flame is necessary, enabling the evaluation of integrals to derive the constants, B_i. Within these constants, B_1 and B_3 correspond to the stabilizing effects of heat and viscous diffusion, respectively, whereas B_2 signifies the stabilizing or destabilizing effect of molecular diffusion.

Another consequence arising from TD instability, aside from the increased folding of the flame, is the localized thinning and acceleration resulting from heightened local combustion activity. Consequently, it is imperative to distinguish between the standard, one-dimensional, laminar, adiabatic quantities (such as flame speed and thickness referred to as S_L and δ_L), which do not account for TD effects, and the laminar, adiabatic, freely propagating values (referred to as S_F and δ_F). These values are obtained through well-resolved multidimensional simulations that explicitly incorporate TD effects.

Howarth et al. [26] asserted that the latter set of values should be regarded as the reference flame speed when employed in combustion sub-models to partially consider the influence of TD effects. Furthermore, Howarth et al. [43] have illustrated that the ω_2 parameter not only proves effective in characterizing TD instability but also facilitates the development of correlations for freely propagating flame speed and flame thickness. These correlations have been established through data fitting from two- and three-dimensional Direct Numerical Simulations carried out across a broad spectrum of operating conditions in a stationary chemical reactor, encompassing a wide range of ω_2 values.

$$S_F = \begin{cases} exp(0.08\cdot\omega_2)\cdot S_L & if \quad p < \Pi_{\text{crit}} \\ (1.+0.47\cdot\omega_2)\cdot S_L & if \quad p > \Pi_{\text{crit}} \end{cases} \tag{9}$$

$$\delta_F = \begin{cases} exp(-0.06\cdot\omega_2)\cdot\delta_L & if \quad p < \Pi_{\text{crit}} \\ \frac{1}{(1+0.26\cdot\omega_2)}\cdot\delta_L & if \quad p > \Pi_{\text{crit}} \end{cases} \tag{10}$$

$$\Pi_{\text{crit}} = \left(\frac{20\cdot\phi}{7-2\cdot\theta}\right)^{\frac{150}{21+10\cdot\theta}} \tag{11}$$

$$\theta = \frac{T}{300} \tag{12}$$

As evident from the equations presented above, two distinct fittings have been proposed, contingent upon the parameter Π_{crit}. This parameter signifies a "ridge" (effectively a two-dimensional surface within the three-dimensional parameter space) where, for a specific temperature and equivalence ratio, there exists a pressure value that yields the maximum level of instability. Consequently, this three-dimensional space can be partitioned into two separate regions.

It is important to note that the thermodynamic conditions experienced during an engine cycle continuously change, leading to possible physically nonsensical discontinuities in the application of Eq. (9). Therefore, within the framework of this study, an alternative functional form, as depicted in Fig. 4, is proposed to describe the transition between the two fitting approaches, effectively eliminating these discontinuities.

$$S_F = exp(0.08\cdot\omega_2)\cdot S_L\cdot(1-\Sigma) + (1.+0.47\cdot\omega_2)\cdot S_L\cdot\Sigma \tag{13}$$

$$\delta_F = exp(-0.06\cdot\omega_2)\cdot\delta_L\cdot(1-\Sigma) + \frac{1}{(1+0.26\cdot\omega_2)}\cdot\delta_L\cdot\Sigma \tag{14}$$

$$\Sigma = 1 - exp\left(-7\cdot\frac{p}{\Pi_{\text{crit}}}\right) \tag{15}$$

Finally, to account for the interaction between TD flame instabilities and turbulence, the freely propagating speed and thickness, referred to as S_s and δ_s, are correlated to the Karlovitz number, as reported in Eqs. (13)–(14) [26]:

$$\frac{S_s}{S_f} = 1 + 0.26\exp\left(-0.038\omega_2\right)\sqrt{Ka} \tag{16}$$

$$\frac{\delta_F}{\delta_s} = 1 + 0.22\exp\left(-0.026\omega_2\right)\sqrt{Ka} \tag{17}$$

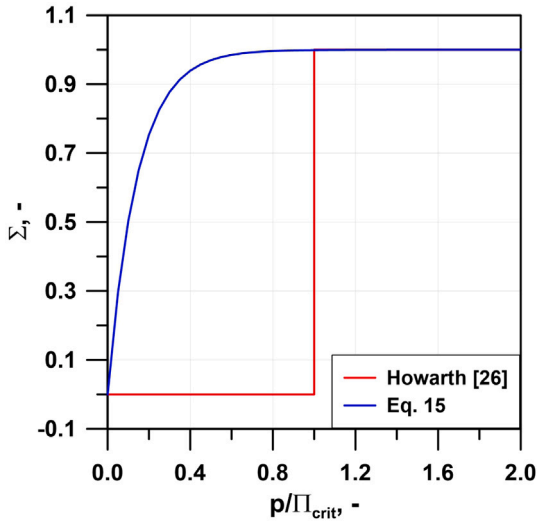

Fig. 4. Σ as a function of $\frac{p}{\Pi_{\text{crit}}}$ according to Howarth [26] and Eq. (15).

3.4. Turbulent combustion modeling

The simulation of turbulent combustion within the engine cylinder involves the integration of phenomenological 0D sub-models for both combustion and turbulence. In the context of the combustion process, the advancement of the flame front within the combustion chamber is represented through a fractal approach, as detailed in previous works [44,45]. In this conceptual framework, the turbulence within the cylinder serves to distort the flame area but does not impact the thickness of the flame front or the laminar flame speed, which are characteristic of the "corrugated flamelet" combustion regime. Based on this assumption, the formulation for the burning rate incorporates an augmentation of the effective flame area relative to the laminar one, quantified by a wrinkling ratio. Meanwhile, the flame front propagates locally at the laminar speed:

$$\left(\frac{dm_b}{dt}\right)_{\text{fractal}} = \rho_u A_T S_L = \rho_u A_L S_L \left(\frac{A_T}{A_L}\right) = \rho_u A_L S_L \Xi \tag{18}$$

The wrinkling factor, Ξ, can be estimated using the following expression, which depends on the fractal dimension, D_3, and the maximum and minimum flame wrinkling scales, L_{max} and L_{min}.

$$\Xi = \left(\frac{L_{\text{max}}}{L_{\text{min}}}\right)^{D_3-2} \tag{19}$$

The above turbulence-dependent parameters are estimated by the K-k-T sub-model, extensively discussed in [32]. However, when considering the effects caused by thermo-diffusive instabilities on hydrogen combustion, the expression of the burn rate is modified and expressed as:

$$\left(\frac{dm_b}{dt}\right)_{\text{w/ TD}} = \rho_u A_L S_s \Xi \tag{20}$$

where the laminar flame speed S_{L} is replaced by the freely propagating speed S_{S}. The flame kernel development is modeled as a temporal delay between the electrical command of the ignition coil and the start of combustion, as detected by an inverse analysis of the experimental

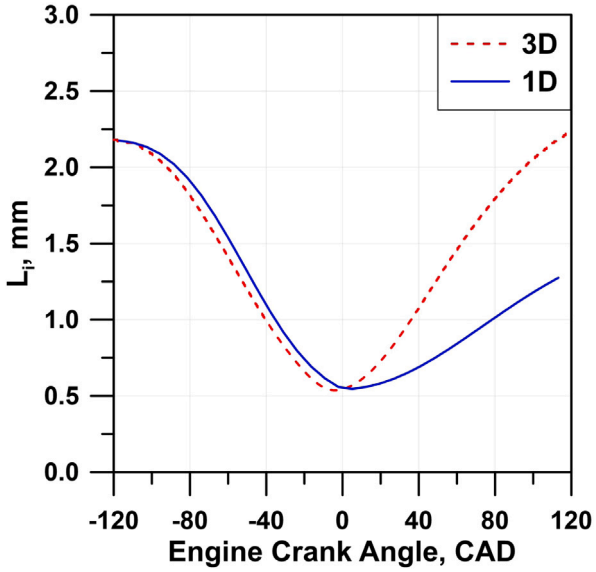

Fig. 5. 3D and 1D integral length scale evolution.

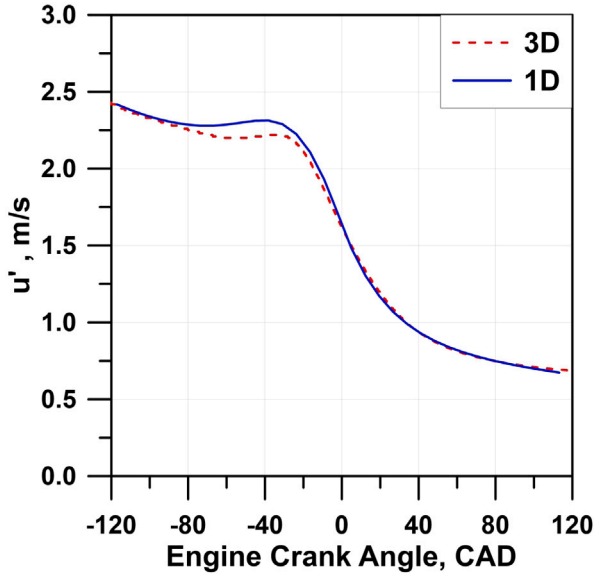

Fig. 6. 3D and 1D turbulent intensity evolution.

pressure cycle. A correlation, valid only for lean mixture, has been developed, which fits the above delay as a function of the in-cylinder temperature, pressure, and air-to-fuel ratio:

$$\tau_k = 3.603 \cdot p^{0.67} \cdot exp(-3572.6/T) \cdot (\lambda - 1)^{3.126} \quad (21)$$

where the pressure is expressed in Pa and the temperature in K. The Eq. (21) allows to estimate the time delay, expressed in ms, between the commanded spark timing and the actual start of the heat release.

4. Results and discussion

4.1. Turbulence model tuning

Figs. 5 and 6 illustrate the comparative analysis of the 3D and 1D models for L_i and u'. Regarding L_i, the compression phase and the region near the TDC emerge as the most crucial phases, with the model

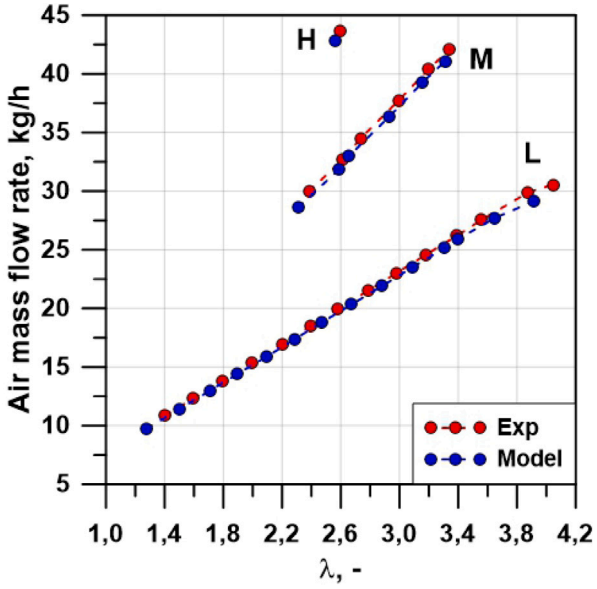

Fig. 7. Experimental/numerical airflow comparison at different loads and λ.

demonstrating a reasonable ability to replicate the 3D CFD data. Some discrepancies become apparent after passing the TDC, but these do not significantly impact the combustion process. Furthermore, Fig. 6 provides a comparison of turbulence intensity between the 1D and 3D simulations. A discernible decrease in turbulence appears between −120 to −60 CAD of the compression stroke, which is caused by the viscous dissipative effects. Notably, the 1D model accurately reproduces the 3D data in this context. Then, turbulence intensifies in the latter half of the compression phase because of the collapse of the tumble vortex. The model adeptly captures this effect in terms of both amplitude and phase. As the TDC is approached, turbulence intensity begins again to diminish due to viscous dissipative effects.

4.2. Engine model validation

Experimental derived boundary conditions to setup the model include intake and exhaust pressure profiles, intake and exhaust mean temperatures, injection timing and fuel mass. As a preliminary step, the tuning process of the parameters controlling the combustion process is carried out to simulate the engine operation under fired conditions. A set of three tuning constants, controlling respectively initial stage, the core, and the completion phase of the combustion (w_{trans}, c_{wrk}, and x_{wc} [46]), is determined through a trial-and-error procedure aiming at faithfully replicating the pressure trace for all 21 test cases in Table 4. In the first part of this section, the numerical–experimental correlation is presented in terms of global engine performance. To this aim, Figs. 7–11 depict the comparison of experimental and calculated engine performance parameters against λ for low (L), medium (M) and high (H) load conditions. The good numerical–experimental agreement for the air mass flow rate indicates the accuracy of both engine geometrical schematization and valve discharge coefficients (Fig. 7). Fig. 8 shows the numerical/experimental comparison of gross IMEP, denoting a satisfactory prediction (average percent error of 2.5%). This derives from the above observations about the engine reconstruction in the 1D framework, together with a reliable prediction of in-cylinder phenomena, especially wall heat transfer and combustion. The largest discrepancy occurs for the points at low load and high λ, with a maximum underestimation of 10%. The same behavior is observed for the Gross Indicated Efficiency (GIE) in Fig. 9. From Fig. 9, it can also

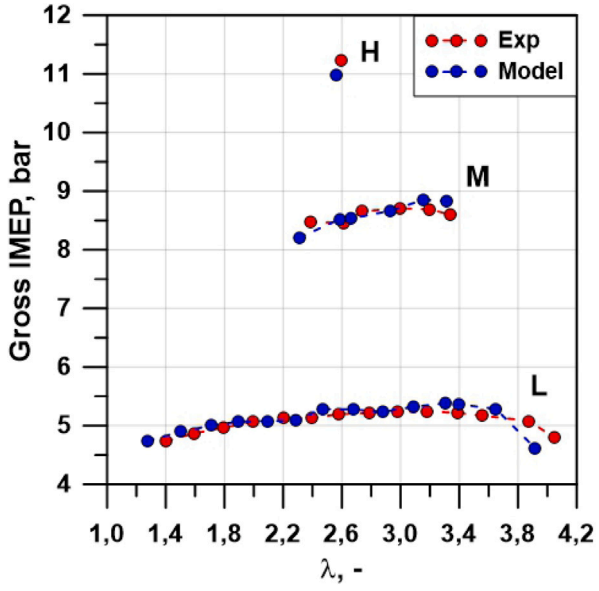

Fig. 8. Experimental/numerical gross IMEP comparison at different loads and λ.

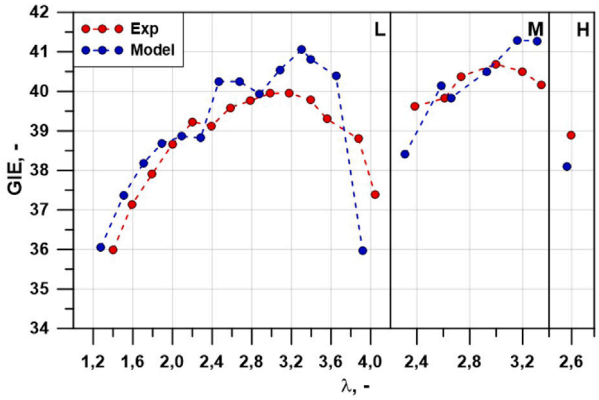

Fig. 9. Experimental/numerical GIE comparison at different loads and λ.

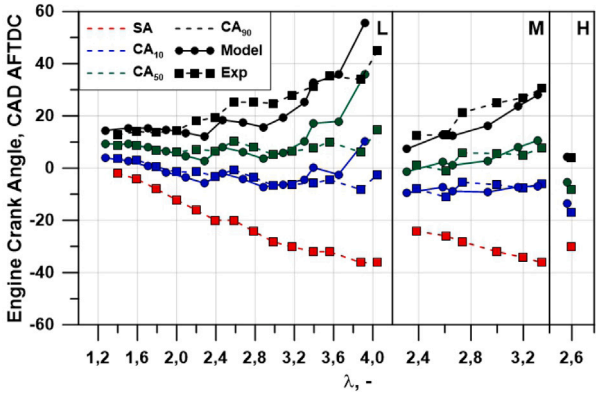

Fig. 10. Experimental/numerical combustion angles comparison at different loads and λ.

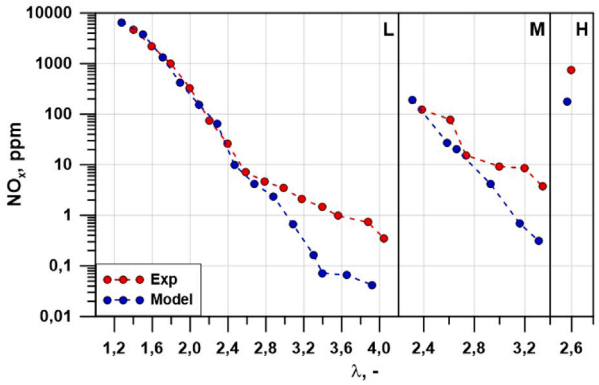

Fig. 11. Experimental/numerical NO_x emissions comparison at different loads and λ.

be inferred that the model is capable of perceiving the physics of the in-cylinder phenomena, leading to an average percent error of 1.6%. As expected, as λ increases, the efficiency increases, reaching a peak of approximately 40% at $\lambda = 3.2$, after which it begins to decrease. This occurs because initially, the lean mixture improves its thermodynamic properties and reduces wall heat losses because of the reduction in in-cylinder temperature. However, subsequently, the detrimental effect of excessive combustion duration becomes predominant, as can be observed from Fig. 10. In this graph, the primary combustion angles are depicted. The CA_{50} is predicted satisfactorily by the code in most cases, with a mean error below 4 CAD. The greatest discrepancies are observed at ultra-lean conditions ($\lambda > 3.6$). The maximum error on CA_{50} for points with λ values below 3.6 is 3.7 CAD, recorded in case #6 as detailed in Table 4. A maximum CA_{50} error of 21 CAD is observed in test case #14 ($\lambda = 4$). The CA_{10} is predicted optimally, and the CA_{90} exhibits a higher error, yet consistently below 10 CAD. It is worth observing the capability of the simulation of detecting the combustion lengthening as λ increases, especially concerning its early stage (from the spark to CA_{10}). Relevant model inaccuracies were only verified for the cases with the highest λ.

The model accurately captures the effect of air–fuel mixture lean-out on NO_x emissions (Fig. 11). According to theoretical expectations, as λ increases NO_x emissions tend to decrease due to the reduced combustion temperature inside the cylinder. The largest discrepancies between the model and the experimental data are observed for λ values where the measured NO_x fall below the instrumental measurement uncertainty, particularly for λ values greater than 3.

The numerical–experimental assessment is in the following presented in terms of pressure cycles and burn rates for some of the test points from Table 4, encompassing low, medium, and high loads at different values of λ (Figs. 12–14). Specifically, the results of two different conditions are compared to illustrate the significance of thermo-diffusive instability effects. The first condition corresponds to a model where thermo-diffusive instabilities affect the laminar flame speed, and it adheres to Eq. (20) (w/ TD). The second condition does not involve accounting for flame corrugation effects using Eq. (1) (w/o TD). It is essential to note that the second variant of the model (w/o TD), due to the absence of the effects of flame corrugation resulting from TD instabilities, utilizes distinct tuning constants compared to the w/TD model. These constants are re-tuned to fit the experimental pressure traces and burn rates for all test points, without any case-by-case adaptation.

Particularly, in Fig. 12, the numerical comparison of in-cylinder pressure traces and burn rate profiles for test case #1-7-13 (Table 4) is presented. It is evident that, owing to the inclusion of TD effects, the burn rates are more accurately replicated by the w/ TD model across various λ values when compared to the w/o TD model. In the case of #13, the reduction in laminar flame speed results in a noticeable

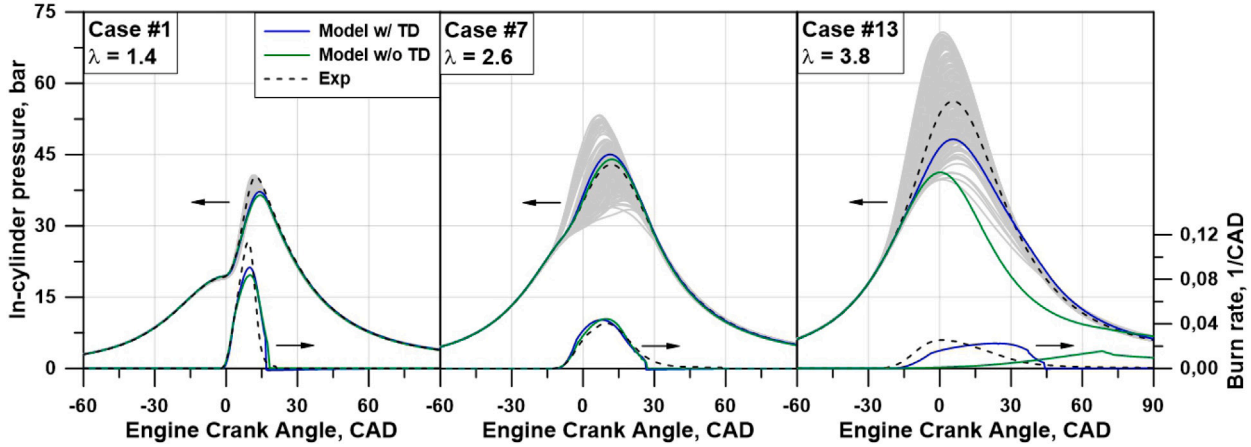

Fig. 12. Experimental/numerical comparison of in-cylinder pressure traces and burn rate profiles for the test case #1-6-12 (Table 4).

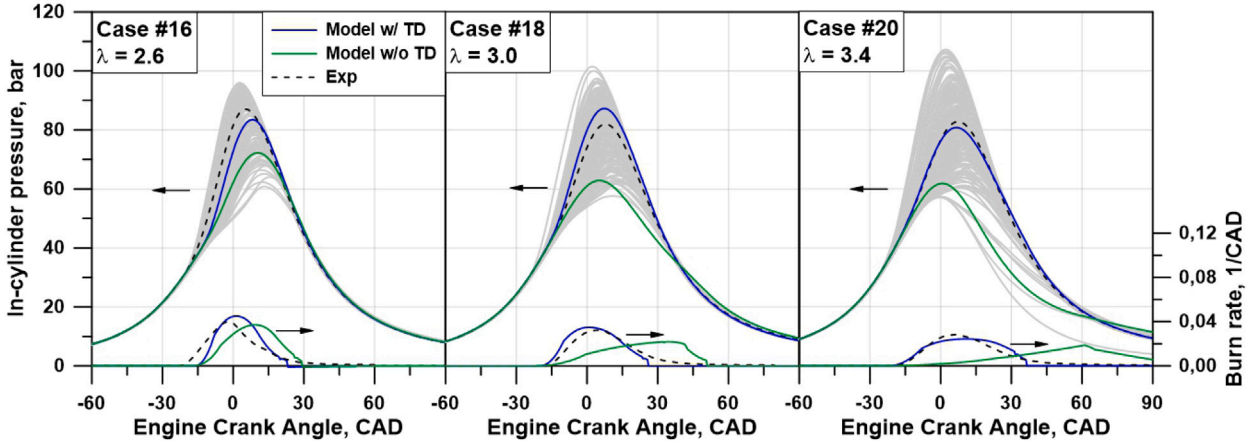

Fig. 13. Experimental/numerical comparison of in-cylinder pressure traces and burn rate profiles for the test case #16-19-20 (Table 4).

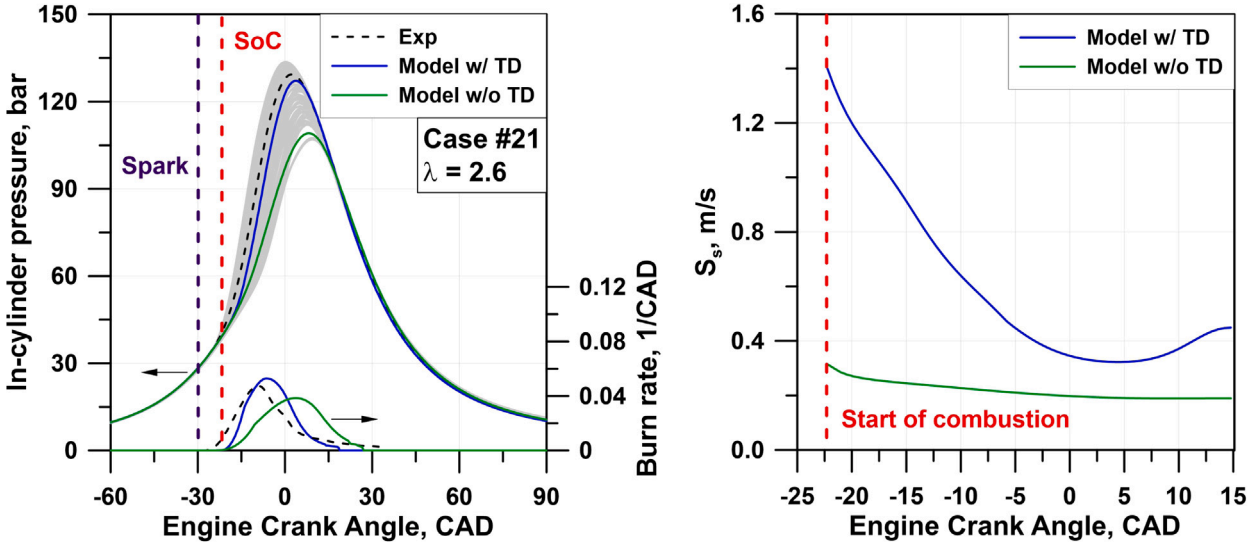

Fig. 14. Experimental/numerical comparison of in-cylinder pressure traces and burn rate profiles for test case #21 (Table 4)(left) and S_u time evolution (right).

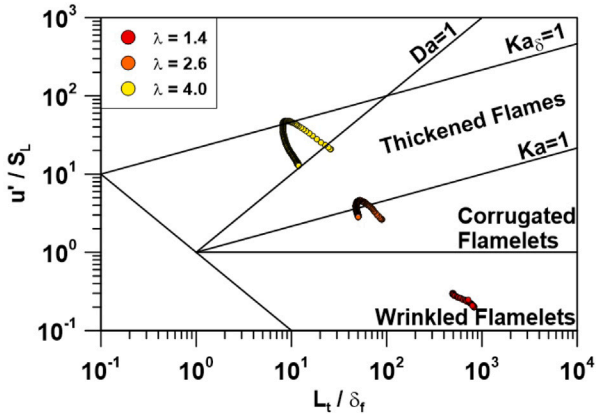

Fig. 15. Borghi diagram for the test cases #1-7-14 (Table 4) during combustion.

underestimation of the burn rate by the w/o TD model. Similarly, a marginal underestimation of the burn rate in the w/ TD model leads to a 7% underestimation of the peak pressure for test case #1.

Similar considerations can be extended to the numerical/experimental comparison of the medium-load test points illustrated in Fig. 13 (case #16-18-20). Once again, the w/ TD model demonstrates its superior capability in capturing the variations in λ. Fig. 14 displays the numerical/experimental comparison for the highest load point (test case #21), along with the temporal evolution of S_s. The slight misalignment of the start of combustion leads to the underestimation of the pressure cycle, and accordingly of the GIE (Fig. 9). It can be noted that the TD instabilities contribute to the increase in S_s throughout the combustion process, consistently higher than the laminar flame speed evaluated by Eq. (1). Indeed, at the combustion start, S_L is relatively low due to reduced in-cylinder temperature and its application for burn rate evaluation leads to relevant underestimation.

The notion that higher λ cases might involve a transition to a different combustion regime is corroborated by examining the Borghi diagram in Fig. 15. This diagram depicts the ratios of characteristic velocities (turbulence intensity relative to laminar flame speed) and lengths (turbulence integral length scale in comparison to flame thickness) throughout the combustion process for three different scenarios. The λ = 1.4 case falls within the wrinkled flamelets regime, where the combustion speed is primarily driven by the laminar flame speed. Indeed, the flame-turbulence interaction is reduced and the TD effects are slightly relevant for lower λ values. Therefore the burn rate underestimation observed in Fig. 12 is mainly a consequence of an underestimated laminar flame speed. It is also evident that most of the points for the λ = 2.6 case fall within the corrugated flamelets regime, where the underlying assumptions of fractal models remain true. When increasing the λ, the combustion process shifts to the up-left part of the Borghi diagram and during the combustion process of test case #14, the combustion regime resides within the broken reaction region, where the fundamental assumptions of the fractal model do not apply. This analysis underscores the imperative need for further model development to achieve a more precise representation of the combustion process in this particular combustion regime.

4.3. Flame instabilities model comparison and recommendation

As discussed in the Introduction section, Ballerini et al. [24] introduced in their engine model the following correlation to enhance the flame speed due to combustion instabilities, developed in [25]:

$$\frac{\left(\frac{S_f}{Sl}\right)-1}{\left(\frac{S_f}{Sl}\right)_{ref}-1}=\left(\frac{\phi}{\phi_{ref}}\right)^{\gamma_\phi}\cdot\left(\frac{T_u}{T_{u,ref}}\right)^{\gamma_{T_u}}\cdot\left(\frac{p}{p_{ref}}\right)^{\gamma_p} \quad (22)$$

where $\left(\frac{S_f}{Sl}\right)$ = 2.6955, ϕ_{ref} = 0.5, γ_ϕ = −1.62, $T_{u,ref}$ = 298 K, γ_{T_u} = −2.56, p_{ref} = 1 bar, γ_p = 0.4. In contrast to the model used in this study, which relies on 3D Direct Numerical Simulations (DNS), Eq. (22) is derived from a fitting of 2D DNS results. As mentioned in [27], the authors noted that hydrogen instabilities are more pronounced in 3D environments compared to 2D, which do not fully account for the diffusion of hydrogen in all directions and underestimate the flame propagation speed. To assess the differences between the two approaches, further simulations are performed where (16) is replaced by Eq. (22), and combustion model constants are tuned again to match at best the experimental data.

For the sake of brevity, only the comparisons of burn rates profile for the test case #1-7-12 (Table 4) using the two different approaches are depicted in Fig. 16. The figure highlights that for λ < 3 the two approaches are equivalent. However, for λ > 3 Eq. (22) underestimates the flame speed. On the contrary, as discussed in the previous section, Eq. (16) can satisfactorily predict the combustion phenomena up to λ = 3.8. These differences are also because Eq. (16), unlike Eq. (22), takes into account the effects of the interaction between flame instabilities and turbulence, a requirement confirmed by the literature [18].

As a general recommendation, due to its simplicity in code implementation and providing the same results as Eq. (16), Eq. (22) should be preferred for cases in which a lower intensity of the flame instabilities or low turbulence are expected (i.e. λ < 3 considering test cases of Table 4). For leaner conditions, Eq. (16) should be used, being able to better perceive the mixture properties and engine operating conditions' effects on the flame instabilities.

5. Conclusion

In this research, a phenomenological combustion model of a hydrogen-fueled PFI SI engine has been developed. To this aim, a model for the estimation of thermo-diffusive instabilities effects on freely propagating flame speed, typical of lean premixed hydrogen combustion, was created. Main steps and outcomes include:

- Development of a novel hydrogen laminar flame speed correlation for ultra-lean combustion (λ up to 4) through chemical calculations of planar steady flames, achieving a coefficient of regression of the fitting of 0.99.
- Model replicated IMEP with an average error of 2.5%, gross indicated efficiency with an average error of 1.6%, main combustion angles with an average error of 3.8 CAD on CA_{50}, and NO_x emissions satisfactorily, showing high sensitivity to operational parameters.
- The assessment of numerical pressure cycles and burn rates with experimental counterparts highlighted the importance of considering thermo-diffusive instabilities effects, particularly at high λ values. Discrepancies were observed at ultra-lean conditions (λ > 3.6) due to the breakdown of the assumptions of the fractal model, since the combustion moves towards the regime of thickened flames. The maximum error on CA_{50} for operating points with λ values below 3.6 is 3.7 CAD, observed in case #6 as listed in Table 4. A maximum CA_{50} error of 21 CAD is achieved for the test case #14 (λ = 4).
- A comparison between the presented approach and the methodology introduced in [24] revealed that, for λ > 3, Eq. (22) tends to underestimate the flame speed. The average error in CA_{50} across all simulated points using the method from [24] increases to 8.1 CAD, in contrast to the 3.8 CAD error observed with the model proposed in this paper. Consequently, as a general recommendation, the model introduced in [24] is preferable for scenarios anticipating lower flame instabilities or reduced turbulence, primarily due to its simpler mathematical formulation and more straightforward code implementation.

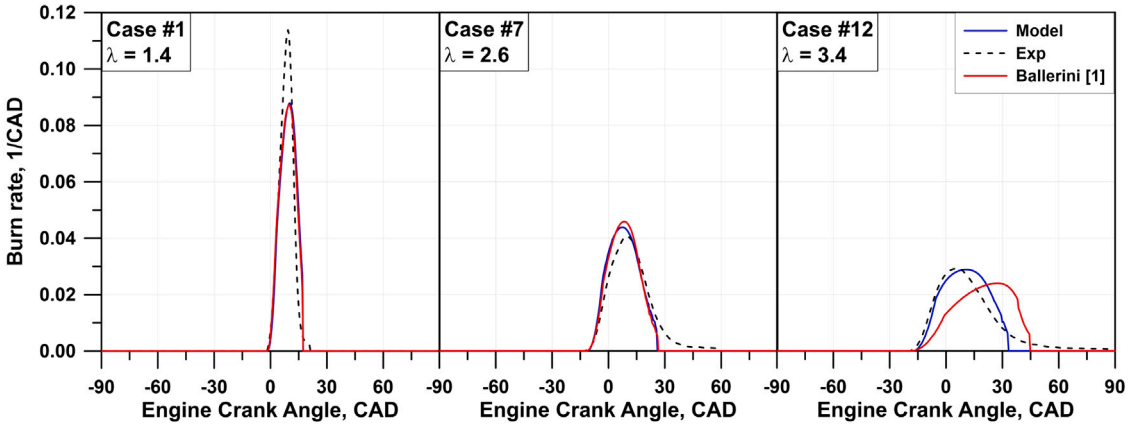

Fig. 16. Comparison of burn rate profiles for the test case #1-9-12 (Table 4) using Eq. (16) (Model in the legend) and Eq. (22) (Ballerini in the legend) [24].

CRediT authorship contribution statement

V. De Bellis: Writing – review & editing, Validation, Supervision, Methodology, Conceptualization. **M. Piras:** Writing – review & editing, Writing – original draft, Visualization, Validation, Investigation, Formal analysis, Data curation, Conceptualization. **F. Bozza:** Writing – review & editing, Supervision, Methodology, Formal analysis, Conceptualization. **E. Malfi:** Writing – review & editing, Visualization, Investigation, Data curation. **R. Novella:** Writing – review & editing, Supervision, Project administration, Methodology, Investigation. **J. Gomez-Soriano:** Writing – review & editing, Supervision, Investigation, Data curation, Conceptualization. **M. Olcina-Girona:** Data curation, Formal analysis, Investigation, Methodology, Visualization, Writing – review & editing.

Declaration of competing interest

The authors declare that they have no known competing financial interests or personal relationships that could have appeared to influence the work reported in this paper.

Data availability

Data will be made available on request.

References

[1] International Energy Agency (IEA). CO2 emissions in 2022. 2022.
[2] Runge P, Sölch C, Albert J, Wasserscheid P, Zöttl G, Grimm V. Economic comparison of electric fuels for heavy duty mobility produced at excellent global sites - a 2035 scenario. Appl Energy 2023;347:121379. http://dx.doi.org/10.1016/j.apenergy.2023.121379, URL https://www.sciencedirect.com/science/article/pii/S0306261923007432.
[3] Millinger M, Reichenberg L, Hedenus F, Berndes G, Zeyen E, Brown T. Are biofuel mandates cost-effective? - an analysis of transport fuels and biomass usage to achieve emissions targets in the European energy system. Appl Energy 2022;326:120016. http://dx.doi.org/10.1016/j.apenergy.2022.120016, URL https://www.sciencedirect.com/science/article/pii/S0306261922012739.
[4] Cabrera-Jiménez R, Mateo-Sanz JM, Gavaldà J, Jiménez L, Pozo C. Comparing biofuels through the lens of sustainability: A data envelopment analysis approach. Appl Energy 2022;307:118201. http://dx.doi.org/10.1016/j.apenergy.2021.118201, URL https://www.sciencedirect.com/science/article/pii/S0306261921014690.
[5] Krause J, Yugo M, Samaras Z, Edwards S, et al. Well-to-wheels scenarios for 2050 carbon-neutral road transport in the EU. 2020, http://dx.doi.org/10.2139/ssrn.4218436.
[6] Ding H, Dong Y, Zhang Y, Yang Y, Wen C. Energy efficiency assessment of hydrogen recirculation ejectors for proton exchange membrane fuel cell (PEMFC) system. Appl Energy 2023;346:121357. http://dx.doi.org/10.1016/j.apenergy.2023.121357, URL https://www.sciencedirect.com/science/article/pii/S0306261923007213.
[7] He Y, Zhou Y, Wang Z, Liu J, Liu Z, Zhang G. Quantification on fuel cell degradation and techno-economic analysis of a hydrogen-based grid-interactive residential energy sharing network with fuel-cell-powered vehicles. Appl Energy 2021;303:117444. http://dx.doi.org/10.1016/j.apenergy.2021.117444, URL https://www.sciencedirect.com/science/article/pii/S0306261921008345.
[8] Fayaz H, Saidur R, Razali N, Anuar F, et al. An overview of hydrogen as a vehicle fuel. Renew Sustain Energy Rev 2012;16:5511–28. http://dx.doi.org/10.1016/j.rser.2012.06.012.
[9] Verhelst S, Wallner T. Hydrogen-fueled internal combustion engines. Prog Energy Combust Sci 2009;35:490–527. http://dx.doi.org/10.1016/j.pecs.2009.08.001.
[10] Li H, Karim G, Sohrabi A. Examination of the oil combustion in a s.I. Hydrogen engine. SAE Tech Pap 2004. http://dx.doi.org/10.4271/2004-01-2916.
[11] Singh A, Pal A, Kumar Gupta N, Kumar Agarwal A. Particulate emissions from laser ignited and spark ignited hydrogen fueled engines. Int J Hydrogen Energy 2017;42:15956–65. http://dx.doi.org/10.1016/j.ijhydene.2017.04.031.
[12] Takagi Y, Oikawa M, Sato R, Kojiya Y, et al. Near-zero emissions with high thermal efficiency realized by optimizing jet plume location relative to combustion chamber wall, jet geometry and injection timing in a direct-injection hydrogen engine. Int J Hydrogen Energy 2019;44:9456–65. http://dx.doi.org/10.1016/j.ijhydene.2019.02.058.
[13] Naganuma K, Honda T, Yamane K, Takagi Y, et al. Efficiency and emissions-optimized operating strategy of a high-pressure direct injection hydrogen engine for heavy-duty trucks. SAE Int J Engines 2010;2:132–40. http://dx.doi.org/10.4271/2009-01-2683.
[14] he Luo Q, Hu J-B, gang Sun B, shui Liu F, Wang X, Li C, zhi Bao L. Effect of equivalence ratios on the power, combustion stability and NOx controlling strategy for the turbocharged hydrogen engine at low engine speeds. Int J Hydrogen Energy 2019;44(31):17095–102. http://dx.doi.org/10.1016/j.ijhydene.2019.03.245, URL https://www.sciencedirect.com/science/article/pii/S0360319919313321.
[15] Rezaei R, Kovacs D, Hayduk C, Mennig M, et al. Euro VII and beyond with hydrogen combustion for commercial vehicle applications: From concept to series development. SAE Tech Pap 2021. http://dx.doi.org/10.4271/2021-01-1196.
[16] Bradley D, Cresswell T, Puttock J. Flame acceleration due to flame-induced instabilities in large-scale explosions. Combust Flame 2001;124(4):551–9. http://dx.doi.org/10.1016/S0010-2180(00)00208-X.
[17] Groff EG. The cellular nature of confined spherical propane-air flames. Combust Flame 1982;48:51–62. http://dx.doi.org/10.1016/0010-2180(82)90115-8, URL https://www.sciencedirect.com/science/article/pii/0010218082901158.
[18] Berger L, Attili A, Pitsch H. Synergistic interactions of thermodiffusive instabilities and turbulence in lean hydrogen flames. Combust Flame 2022;244:112254. http://dx.doi.org/10.1016/j.combustflame.2022.112254, URL https://www.sciencedirect.com/science/article/pii/S0010218022002693.
[19] Ye Y, Gao W, Li Y, Zhang P, Cao X. Numerical study of the effect of injection timing on the knock combustion in a direct-injection hydrogen engine. Int J Hydrogen Energy 2020;45(51):27904–19. http://dx.doi.org/10.1016/j.ijhydene.2020.07.117, URL https://www.sciencedirect.com/science/article/pii/S0360319920326926.
[20] Klepatz K, Rottengruber H, Zeilinga S, Koch D, et al. Loss analysis of a direct-injection hydrogen combustion engine. SAE technical paper (2018-01-1686), 2018, http://dx.doi.org/10.4271/2018-01-1686.
[21] Koch DT, Sousa A, Bertram D. H2-engine operation with EGR achieving high power and high efficiency emission-free combustion. SAE technical paper (2019-01-2178), 2019, URL https://doi.org/10.4271/2019-01-2178.
[22] Millo F, Piano A, Rolando L, Accurso F, Gullino F, Roggio S, Bianco A, Pesce F, Vassallo A, Rossi R. Synergetic application of zero-, one-, and three-dimensional computational fluid dynamics approaches for hydrogen-fuelled spark ignition

engine simulation. SAE Int J Engines 2021;15(4):561–80. http://dx.doi.org/10.4271/03-15-04-0030, URL https://www.sae.org/publications/technical-papers/content/03-15-04-0030/. Number: 03-15-04-0030.

[23] Piano A, Millo F, Quattrone G, Pesce F, Vassallo A. Comprehensive quasi-dimensional model to predict combustion process, knock likelihood and cycle-by-cycle variability in a hydrogen-fueled internal combustion engine. SAE technical paper 2023-32-0171, Warrendale, PA: SAE International; 2023, http://dx.doi.org/10.4271/2023-32-0171, URL https://www.sae.org/publications/technical-papers/content/2023-32-0171/. ISSN: 0148-7191, 2688-3627.

[24] Ballerini A, Cerri T, Marinoni AM, Onorati A. Advances in 1D thermo-fluid dynamic simulation of SI hydrogen-fueled engine. J Phys Conf Ser 2022;2385(1):012055. http://dx.doi.org/10.1088/1742-6596/2385/1/012055.

[25] Berger L, Attili A, Pitsch H. Intrinsic instabilities in premixed hydrogen flames: parametric variation of pressure, equivalence ratio, and temperature. Part 2 – non-linear regime and flame speed enhancement. Combust Flame 2022;240:111936. http://dx.doi.org/10.1016/j.combustflame.2021.111936, URL https://www.sciencedirect.com/science/article/pii/S0010218021006799.

[26] Howarth TL, Aspden AJ. An empirical characteristic scaling model for freely-propagating lean premixed hydrogen flames. Combust Flame 2022;237:111805. http://dx.doi.org/10.1016/j.combustflame.2021.111805, URL https://www.sciencedirect.com/science/article/pii/S0010218021005484.

[27] Howarth TL, Hunt EF, Aspden AJ. Thermodiffusively-unstable lean premixed hydrogen flames: Phenomenology, empirical modelling, and thermal leading points. Combust Flame 2023;253:112811. http://dx.doi.org/10.1016/j.combustflame.2023.112811, URL https://www.sciencedirect.com/science/article/pii/S001021802300192X.

[28] Molina S, Ruiz S, Gomez-Soriano J, Olcina-Girona M. Impact of hydrogen substitution for stable lean operation on spark ignition engines fueled by compressed natural gas. Res Eng 2023;17:100799. http://dx.doi.org/10.1016/j.rineng.2022.100799, URL https://www.sciencedirect.com/science/article/pii/S2590123022004698.

[29] Climent H, Dolz V, Pla B, González-Domínguez D. Analysis on the potential of EGR strategy to reduce fuel consumption in hybrid powertrains based on advanced gasoline engines under simulated driving cycle conditions. Energy Convers Manage 2022;266:115830.

[30] Pochet M, Jeanmart H, Contino F. Uncertainty quantification from raw measurements to post-processed data: A general methodology and its application to a homogeneous-charge compression–ignition engine. Int J Engine Res 2020;21(9):1709–37. http://dx.doi.org/10.1177/1468087419892697, arXiv:https://doi.org/10.1177/1468087419892697.

[31] Bellis VD, Bozza F, Fontanesi S, Severi E, Berni F. Development of a phenomenological turbulence model through a hierarchical 1D/3D approach applied to a VVA turbocharged engine. SAE Int J Engines 2016;9(1):506–19, URL http://www.jstor.org/stable/26284835.

[32] De Bellis V, Severi E, Fontanesi S, Bozza F. Hierarchical 1D/3D approach for the development of a turbulent combustion model applied to a VVA turbocharged engine. Part I: Turbulence model. Energy Procedia 2014;45:829–38. http://dx.doi.org/10.1016/j.egypro.2014.01.088, URL https://www.sciencedirect.com/science/article/pii/S1876610214000897. ATI 2013 - 68th Conference of the Italian Thermal Machines Engineering Association.

[33] Broatch A, Novella R, García-Tíscar J, Gomez-Soriano J, Pal P. Investigation of the effects of turbulence modeling on the prediction of compression-ignition combustion unsteadiness. Int J Engine Res 2022;23(4):541–59. http://dx.doi.org/10.1177/1468087421990478, arXiv:https://doi.org/10.1177/1468087421990478.

[34] Berni F, Cicalese G, Borghi M, Fontanesi S. Towards grid-independent 3D-CFD wall-function-based heat transfer models for complex industrial flows with focus on in-cylinder simulations. Appl Therm Eng 2021;190:116838.

[35] Issa RI. Solution of the implicitly discretised fluid flow equations by operator-splitting. J Comput Phys 1986;62(1):40–65.

[36] Gomez-Soriano J, Sapkota P, Wijeyakulasuriya S, D'Elia M, Probst D, Viswanathan V, Olcina-Girona M, Novella R. Numerical modeling of hydrogen combustion using preferential species diffusion, detailed chemistry and adaptive mesh refinement in internal combustion engines. SAE Tech Pap 2023.

[37] Novella R, Pastor J, Gomez-Soriano J, Barbery I. Effects of pre-chamber flow-field on combustion stability in a spark-ignition engine using large-eddy simulations. Phys Fluids 2023;35(11).

[38] Ramognino F, Sforza L, D'Errico G, Gomez-Soriano J, Onorati A, Novella R. CFD modelling of hydrogen-fueled SI engines for light-duty applications. SAE Tech Pap 2023.

[39] Konnov AA. Yet another kinetic mechanism for hydrogen combustion. Combust Flame 2019;203:14–22. http://dx.doi.org/10.1016/j.combustflame.2019.01.032, URL https://www.sciencedirect.com/science/article/pii/S0010218019300501.

[40] Landau L. On the theory of slow combustion. In: Pelcé P, editor. Dynamics of curved fronts. Academic Press; 1988, p. 403–11. http://dx.doi.org/10.1016/B978-0-08-092523-3.50044-7, URL https://www.sciencedirect.com/science/article/pii/B9780080925233500447.

[41] Matalon M, Cui C, Bechtold JK. Hydrodynamic theory of premixed flames: effects of stoichiometry, variable transport coefficients and arbitrary reaction orders. J Fluid Mech 2003;487:179–210. http://dx.doi.org/10.1017/S0022112003004683, Publisher: Cambridge University Press.

[42] Matalon M. The Darrieus–Landau instability of premixed flames. Fluid Dyn Res 2018;50(5):051412. http://dx.doi.org/10.1088/1873-7005/aab510, Publisher: IOP Publishing.

[43] Howarth T, Hunt E, Aspden A. Thermodiffusively-unstable lean premixed hydrogen flames: Phenomenology, empirical modelling, and thermal leading points. Combust Flame 2023;253:112811. http://dx.doi.org/10.1016/j.combustflame.2023.112811, URL https://www.sciencedirect.com/science/article/pii/S001021802300192X.

[44] Gouldin F. An application of fractals to modeling premixed turbulent flames. Combust Flame 1987;68(3):249–66. http://dx.doi.org/10.1016/0010-2180(87)90003-4.

[45] Bozza F, Gimelli A, Merola S, Vaglieco B. Validation of a fractal combustion model through flame imaging. SAE technical paper, no. 2005-01-1120, 2005, http://dx.doi.org/10.4271/2005-01-1120.

[46] Tufano D. A quasi-dimensional SI combustion model: a bi-fractal approach. Energy Procedia 2017;126:931–8. http://dx.doi.org/10.1016/j.egypro.2017.08.166, URL https://www.sciencedirect.com/science/article/pii/S1876610217336597. ATI 2017 - 72nd Conference of the Italian Thermal Machines Engineering Association.